Nanoscale Imaging of Plasmonic Hot Spots and Dark Modes with the Photothermal Induced Resonance Technique

Basudev Lahiri[1, 2], *Glenn Holland*[1], *Vladimir Aksyuk*[1] *and Andrea Centrone* [1, 2]*

[1]NIST, Center for Nanoscale Science and Technology, Gaithersburg, 100 Bureau Drive, MD 20899 (USA)

[2]University of Maryland, Institute for Research in Electronics and Applied Physics (IREAP), College Park, MD 20742 (USA)

KEYWORDS: SEIRA, PTIR, plasmonic resonators, hot spots, dark mode, infrared spectroscopy.

ABSTRACT

The collective oscillation of conduction electrons, responsible for the LSPRs, enables engineering nanomaterials by tuning their optical response from the visible to THz as a function of nanostructure size, shape and environment. While theoretical calculations helped tremendously in understanding plasmonic nanomaterials and optimizing their light matter-interaction, only a few experimental techniques are available to study these materials with high spatial resolution. In this work, the Photo Thermal Induced Resonance (PTIR) technique is

applied for the first time to image the dark plasmonic resonance of gold Asymmetric Split Ring Resonators (A-SRRs) in the mid-infrared (IR) spectral region with nanoscale resolution. Additionally, the chemically-specific PTIR signal is used to map the local absorption enhancement of polymethylmethacrylate (PMMA) coated on A-SRRs, revealing hot spots with local enhancement factors up to ≈ 30 at 100 nm lateral resolution. We argue that PTIR nanoscale characterization will facilitate the engineering and application of plasmonic nanomaterials for mid-IR applications.

Localized surface plasmon resonances (LSPR) couple propagating light waves with nanoscale volumes of matter (hot spots"), enabling new applications in fields like energy,[1] sensing,[2-4] and therapeutics.[5, 6] The enhanced local light-matter interaction is exploited for example by surface-enhanced spectroscopies for sensitive detection.[7-13] The recent development of plasmonic nanostructures with resonances in the mid-IR has generated considerable interest in Surface-Enhanced Infrared Absorption (SEIRA) Spectroscopy,[11-17] due to chemical detection limits in the zeptomolar range.[12] SEIRA enhancement factors in the order of 10^3 to 10^5 have been calculated for very small hot spots[11, 12, 16] but the diffraction of the long IR wavelengths (2.5 μm to 20 μm) has so far prevented the direct determination of SEIRA enhancement factors with nanoscale resolution.

Theoretical calculations are routinely used to understand the optical properties of plasmonic nanomaterials but only few experimental techniques are available to study these materials with high spatial resolution.[18-23] For example, scattering scanning near field optical microscopy (s-SNOM) have been successfully applied to map the near field of optical antennas[22-25] and to image bright and dark modes of plasmonic structures.[21] s-SNOM measures the amplitude and phase of the light scattered by a sharp metallic tip in proximity of a sample. The scattered light

field is a complex function of both the sample local extinction coefficient (κ) and the real part of the refractive index (n), together with the dielectric properties and the geometry of the probe. This makes the identification of unknown materials a challenging task that requires theoretical modeling[26] to describe the tip-sample-substrate interactions in the near field. A less invasive technique where the probe does not interact with the near field of the plasmonic structures, and/or that allows determining the chemical composition directly and without a precise model of the probe's geometry and optical properties is desirable.

PTIR combines the lateral resolution of Atomic Force Microscopy (AFM) with the chemical specificity of IR Spectroscopy.[27-31] Samples are placed on an optically transparent prism and illuminated with a tunable IR pulsed laser in a total internal reflection configuration to minimize direct light-tip interaction (Fig.1a). The absorption of a laser pulse by the sample results in local heating, sample expansion, and mechanical excitation of the AFM cantilever in contact with the sample. The low repetition rate of the laser (1 kHz) assures that a new pulse will excite a sample and cantilever after they have returned to equilibrium. While the typical laser spot size is about ≈ 30 μm, the AFM tip acts as a "spatial filter" (Fig. 1c) allowing the extraction of spectroscopic information with nanoscale spatial resolution, several times smaller than the diffraction limit of IR light.[28, 31, 32] The local infrared spectrum is obtained by plotting the maximum amplitude of the tip deflection (Fig. 1b) as a function of the optical frequency. Notably, the PTIR signal (Fig. 1b) is proportional to the absorbed energy[31] (not scattering) and the PTIR spectra are directly comparable with IR spectral libraries,[28] allowing materials identification. PTIR chemical images are obtained by illuminating the sample at a constant frequency while scanning the AFM tip.[29-31] Given the signal transduction chain, the PTIR signal is proportional to the sample linear expansion coefficient (α) and inversely proportional to the sample thermal conductivity (η)[30, 33]

thus making polymers[28, 29] or biological samples[29, 32] (large α and small η) easier to measure. While PTIR measurements on inorganic dielectrics (small α and small η) are challenging but possible,[27] metallic structures (small α and large η) have yet to be measured with the PTIR technique. In this work, we rely on the large linear thermal expansion coefficient of PMMA films coating gold plasmonic resonators to mechanically amplify, and measure for the first time, the PTIR signal originating from the absorption in metallic structures.

A-SRRs are plasmonic nanostructures composed of metallic rings split asymmetrically into two separate arcs.[4] Changing the diameter of the resonators allows tuning their LSPR (figure 2a, S1) across the whole IR spectral range to match the vibrational absorption resonances of target analytes.[4] The degree of asymmetry controls the electrical dipolar coupling of the A-SRRs dark-mode[4, 34, 35] to the propagating waves and maximizes the field intensity in the resonator "hot spots". "Hot spot" engineering is the subject of intense research mostly relying on theoretical modeling,[11, 34-36] and only recently the direct experimental verification of the dark-mode excitation has been provided.[21] Here we employ the PTIR technique to directly visualize SEIRA hot spots and the A-SRRs dark-mode with nanoscale lateral resolution, corroborating theoretical predictions and our own finite-element modeling. We name this technique Surface-Enhanced PTIR (or SE-PTIR) and we demonstrate its utility for engineering plasmonic nanomaterials towards their technological applications.

The gold A-SRRs arrays studied here were fabricated on top of Zinc Selenide (ZnSe) prisms with a combination of electron beam lithography and metal lift-off techniques[31] (Fig. S2). The A-SRRs have a strip width of 375 nm ± 10 nm, a thickness of 150 nm ± 10 nm and an external diameter between 1050 nm (± 25 nm) and 2150 nm (± 25 nm), resulting in resonance frequencies in the region from 3.5 μm to 11 μm (Fig. 2a, S1). The A-SRRs were arranged in square arrays

with a pitch of approximately twice the A-SRRs diameter (hereafter named ASRR-xxx-d, fig. 2b and S3) or of 10 μm (hereafter named ASRR-xxx-10, Fig S4), where xxx indicates the resonator external diameter in nm. The resonators were coated with a 200 nm PMMA layer, used as a probe to measure the absorption enhancement.

In analogy with the molecular orbital theory, hybridization is a useful concept for understanding the plasmonic modes of interacting nanostructures.[37, 38] The fundamental modes of two near-identical arcs in close proximity hybridize, forming symmetric and antisymmetric collective modes (fig. 3a). The higher-energy symmetric "bright" mode has a large net electric dipole, and interacts strongly with the incident light because the electric polarization vectors are in phase in the two arcs. The lower-energy antisymmetric "dark" mode,[36] also referred in the literature as a "trapped" mode,[35] has electric polarization vectors of opposite phase in the two arcs (fig. 3a). In the limiting case of two identical arcs, such antisymmetric mode has zero net electric dipole moment and can't be excited by surface-normal illumination. The reduced coupling, controlled by the resonator geometry, lowers the scattering losses, resulting in a narrower resonance and potentially stronger enhancement. The constructive and destructive interference of the broader bright-mode with the narrower dark-mode leads to maxima and a minimum in the resonators reflection spectra (Fig. 2a, S1). Excitation of these plasmonic modes is strongly polarization dependent: for linear polarization of a normally incident plane wave, stronger coupling is obtained with electric field parallel to the long direction of the arcs (hereafter parallel polarization, fig 2b-c), while for the perpendicular polarization the coupling is forbidden by symmetry (fig 2c).

Finite-Element-Method (FEM) calculations suggest that under the conditions of PTIR experiments, the energy dissipated in the arcs is mostly due to the dark-mode (Fig 3b insets). In

particular, at longer wavelength only the dark-mode is excited wherein a larger fraction of the optical power is dissipated by the longer arc. At shorter wavelengths, a small admixture of the bright-mode increases the power dissipated by the short arc and suppresses the power dissipated by the long arc via constructive and destructive interference (Fig. 3b insets). This numerically predicted wavelength-dependent crossover (Fig 3b) is observed experimentally in the PTIR images for the ASRR-1300-d array recorded at frequencies absorbed by the arcs but not by PMMA. The PTIR images of the plasmonic resonances for the underlying A-SRRs structures (fig 3d-g) were measured despite the fact that the AFM height image (fig. 3d) can barely identify the location of the resonators under the PMMA layer. These PTIR images (Fig. 3e-g) represent the energy dissipated within the arcs due to the plasmon excitation[4] and provide evidence of the interference between the two modes. The crossover in the power dissipation between the two arcs is calculated at around 5.5 um (fig 3b) in rather good agreement with the experimentally observed crossover around 5.43 um (fig 3f). The efficient excitation of the dark-mode (> 25 % of incident power is absorbed, Fig. 3b), is qualitatively attributed to a constructive combination of electric and magnetic dipolar coupling of the dark-mode to the plane wave incident at 45° from the ZnSe side, specifically from the short arc direction. The plasmonic modes of ASRR-1700-d and ASRR-1650-d are reported in figure S5 and S6 of the supporting information, respectively. These measurements were obtained for wavelengths not absorbed by PMMA, whose role is merely to mechanically amplify the signal from the plasmonic mode absorption. For wavelengths where the direct vibrational absorptions of PMMA occur the PTIR plasmonic mode signal is overwhelmed by the PMMA signal due to the strong absorption enhancement in the near-field hot spots, as discussed below.

The far-field FTIR spectra are a measure of the resonators' spectral response, which depends on the PMMA dielectric constant (fig. S7). Near PMMA vibrational absorption lines both real and imaginary parts of the PMMA dielectric constant vary,[39] modulating the resonator response in a complex fashion as previously observed in SEIRA spectra.[4, 11, 12, 17] This modulation results in peaks and dips in the FTIR reflection spectra (fig. S8a), complicating the identification of unknown analytes. In contrast, since the PTIR signal depends directly only on absorption (not scattering),[31] the SE-PTIR signal is proportional to the product of PMMA absorption and the near-field optical power density. As long as the resonator response modulation remains shallow, the optical power density does not vary strongly within any single peak line width, and the peaks in the SE-PTIR spectra coincide with the PMMA peaks (fig. S8b) with no distortion or significant shift as experimentally observed.

Despite relatively low average volumetric enhancements for sparse plasmonic structures, calculations predict strong localized enhancements in the near-field[11, 12] determined by the plasmonic mode shape and by the "lighting rod" effect combined with the resonator coupling efficiency to the far-field. The AFM height and PTIR images for ASRR-1700-d (fig 4) recorded for PMMA vibrational absorptions frequencies show hot-spots close to the A-SRRs arc terminations (fig.4). Since the PTIR intensity is proportional to the absorbed energy[31] the PTIR maps represent the direct image of the local absorption enhancement in the near-field. The observed hot spots are clearly consistent with the numerically calculated electric field in the PMMA layer enhanced in the gap between the arcs (fig 3b). Additionally, PTIR data on arrays with small pitch and short resonant wavelength (ASRR-1150-d, Fig. S9) show the hot spots becoming more diffuse and overlapping with those of the neighboring rings at longer excitation wavelengths. PTIR data from the ASRR-1300-d are reported in figure S10.

PTIR images and spectra of PMMA coated A-SRR-2000-10 are reported in fig. 5 and fig. S11. By comparing the PMMA spectra taken on a hot spot and 300 μm away from the A-SRR array (figure 5d) local enhancement factors up to 28 were measured. We estimate that such enhancement arises from a volume of $6.3 \cdot 10^{-3}$ μm^3 or smaller. Even larger signal enhancements (> 50) were obtained by increasing the laser energy per pulse (up to 1 μJ, figure S12); however, in these conditions the thermo-mechanical detected signal was outside its linear range, possibly because the surface enhanced absorption in the hot spots may cause the PMMA transient temperature to be above the polymer glass transition temperature at selected wavelengths (where the enhancement is stronger). As expected, the interaction with the perpendicular polarization is much weaker but hot spots are still identifiable in the near-field (fig. S13). In this case not all spots are confined in the gaps between the arcs.

In conclusion, we have demonstrated the utility of PTIR for studying the near-field properties of plasmonic nanomaterials. The dark (trapped) mode in A-SRR structures was experimentally visualized by mapping with nanoscale spatial resolution the electromagnetic dissipation in the resonators, as well as, separately, in the surrounding dielectric. The SE-PTIR spectra and images reveal hot spots with large absorption enhancement in the resonator gaps. We believe that the high chemical sensitivity and high lateral resolution of SE-PTIR will be useful for the development of plasmonic materials and metamaterials for applications requiring enhanced light-matter interaction[40] at the nanoscale like sensing, therapeutics and energy.

Experimental

Sample fabrication. All chemicals were used as received without further purification. A-SRRs arrays were fabricated directly on ZnSe prisms as follows (see fig S2). The prisms were

cleaned in an ultrasonic bath with acetone (1 min) and methanol (1 min). A bilayer of PMMA positive electron beam resist (PMMA) was spun (25 Hz) on top of the prism, using a custom polyphenylsulfone adaptor piece, as described previously.[31] The resist was baked in an oven (140 °C for 30 min) before depositing an aluminum charge dissipation layer (30 nm ± 5 nm) with an electron-beam evaporator. Electron beam lithography (EBL) was used to write the A-SRRs arrays directly on the ZnSe prisms by mean of a custom adaptor piece.[31] The electron beam dose was varied from 1350 μC/cm^2 to 1600 μC/cm^2 depending on the A-SRRs diameter and array pitch. Square A-SRRs arrays (300 μm by 300 μm) were written for each A-SRRs diameter. Next, the aluminum layer was removed with a tetramethylammonium hydroxide, water solution (2.4 % volume fraction) and the pattern was developed in a mixture of Methyl Iso-butylketone (MIBK) and isopropyl alcohol (IPA). Electron beam deposition was used to deposit (0.1 nm/s at 6.67 · 10^{-4} Pa) a thin chromium adhesion layer (≈ 5 nm) and a gold layer (150 nm ± 10 nm). Finally, the A-SRRs arrays were obtained after lift of in hot acetone (45 °C). Arrays with the same resonator diameter and pitch were fabricated in two orientations rotated by 90°. The A-SRR arrays were characterized before and after spinning at 35 Hz (2100 rpm) a PMMA film (≈ 200 nm ± 10 nm) on top of the resonators.

FTIR spectroscopy. Fourier Transform Infrared (FTIR) spectra were recorded at near normal incidence (fig. S10a) with an FTIR spectrometer equipped with an infrared microscope by illuminating a 200 μm by 200 μm sample area with a 36x reverse Cassegrain reflection objective (NA = 0.52) and a ZnSe wire grid polarizer (to control the light polarization). The 36x reflective objective construction provides illumination and collection of light with incidence angles from 15° to 30° from sample surface normal (see Fig S14); the light between normal incidence and

15° is blocked by the objective. 128 spectra (4 cm^{-1} resolution) were acquired and averaged for each sample.

PTIR Experimental set up. PTIR experiments were carried out using a commercial PTIR setup which consists of an AFM microscope operating in contact mode and a tunable pulsed laser source consisting of an Optical Parametric Oscillator (OPO) based on a non-critically phase-matched $ZnGeP_2$ crystal. The laser emits pulses 10 ns long at 1 kHz repetition rate which are tunable from 4000 cm^{-1} to ≈ 1025 cm^{-1} (from 2.5 μm to 9.76 μm). The maximum energy per pulse used was 0.4 μJ for the SE-PTIR experiments and 2 μJ for imaging resonator modes, unless otherwise noted (figure S12). The samples on a ZnSe prism were illuminated in total internal reflection (fig. 1a) by focusing the laser light under the AFM tip with a ZnSe lens. The typical spot size is 30 μm ± 10 μm depending on the wavelength. The laser output is linearly polarized and a rotating ZnSe wire grid linear polarizer is used as a variable attenuator to control the light intensity. A polarization control module, consisting of three motorized mirrors, is used to obtain the desired polarization at the sample. Most of the optics in the PTIR setup and inside the laser are placed on motorized stages which allow automatic wavelength selection and sweeping via a computer interface. Since different wavelengths are typically emitted by the OPO at different angles, an infrared pyroelectric camera was used to calibrate the mirror positions resulting in the laser output co-linearity in the entire wavelength range.

PTIR experiments. PTIR spectra were obtained by averaging the cantilever deflection amplitude from 256 individual laser pulses at each wavelength and tuning the laser at intervals of 3 cm^{-1}. PTIR images were recorded by illuminating the sample with a constant wavelength while scanning the AFM tip. The AFM height and the PTIR signal acquisition was synchronized so that for each AFM pixel the PTIR signal is an average over a fixed number of laser pulses[31] (32

or 64 in this work). The pixel sizes are 40 nm x 40 nm unless otherwise noted. All PTIR experiments were recorded with linearly, s-polarized light with the electric field vector always in the A-SRR array plane and perpendicular to the plane of incidence (blue arrow of figure S10 b,c). Arrays with the same resonator diameter and pitch were fabricated on top of ZnSe prisms in two orientations rotated by 90°. The PTIR data for parallel and perpendicular polarizations mentioned in the text are obtained on differently oriented structures with incident polarization unchanged (figure S14c). For all experiments with parallel polarization the sample illumination direction occurred from the resonators short arc. Commercially available 450 μm long silicon contact-mode AFM probes with a nominal spring constant between 0.07 N/m and 0.4 N/m were used for this study.

FEM calculations. FEM modeling of light interacting with the ASRR-1300-d sample was conducted using commercial finite element software to solve Maxwell's equations in the frequency domain in 3 dimensions (3D). The 3D model included one array period centered on the ASRR gold (plus thin chromium adhesion layer) structure, ZnSe dielectric under the resonator, PMMA dielectric above and around the resonator and air above PMMA. For simplicity, a planarized layer of PMMA was used, with the top planar surface parallel to the ZnSe surface. The model included a 3 μm thick ZnSe region and 2.8 μm thick air region, both of which were terminated by perfectly matched layers to simulate open boundaries on top and bottom. Periodic boundary conditions were used for the sides of the single array element, with field continuity condition of the boundaries parallel to the plane of incidence and Floquet periodicity condition on the side boundaries perpendicular to the plane of incidence. The Floquet periodicity phase difference was chosen corresponding to the specific angle and wavelength of incident plane wave illumination and whether illumination was from the air ("top") or ZnSe

("bottom") side. The model volume was discretized with a variable density tetrahedral mesh. Dielectric properties for different regions were: air n = 1, ZnSe n = 2.5, PMMA n = 1.4 (neglecting PMMA absorption lines). For Au, tabulated values for the real and imaginary part of the dielectric constant were used, and Drude model was used for Cr with $\omega = 35000$ cm^{-1} and $\Gamma = 1500$ cm^{-1}. Solutions were obtained at multiple optical frequencies corresponding to vacuum wavelength from 3 μm to 9 μm for parallel incident polarization, either from the air-side (for surface-normal plane wave illumination, results in Fig 3a) or from the ZnSe-side (for 45° plane wave illumination incident from the direction of the short arc, Fig 3b). Ohmic losses and electric polarizations were integrated over the individual arc volumes using the obtained solutions, while the electric field vectors and vertical polarization maps in Fig. 3 are plotted in the horizontal plane 100 nm above the ZnSe surface.

Scanning Electron Microscope (SEM) images. SEM images were used to measure the A-SRRs dimensions and pitch. Images were acquired with commercial Scanning Electron Microscope with 5 kV acceleration voltage and with 5 mA of current. Samples were sputter-coated with a 10 nm layer of gold/palladium alloy using a sputter tool under vacuum (1.3×10^{-2} Pa). The uncertainties in the A-SSRs dimension correspond to a standard deviation.

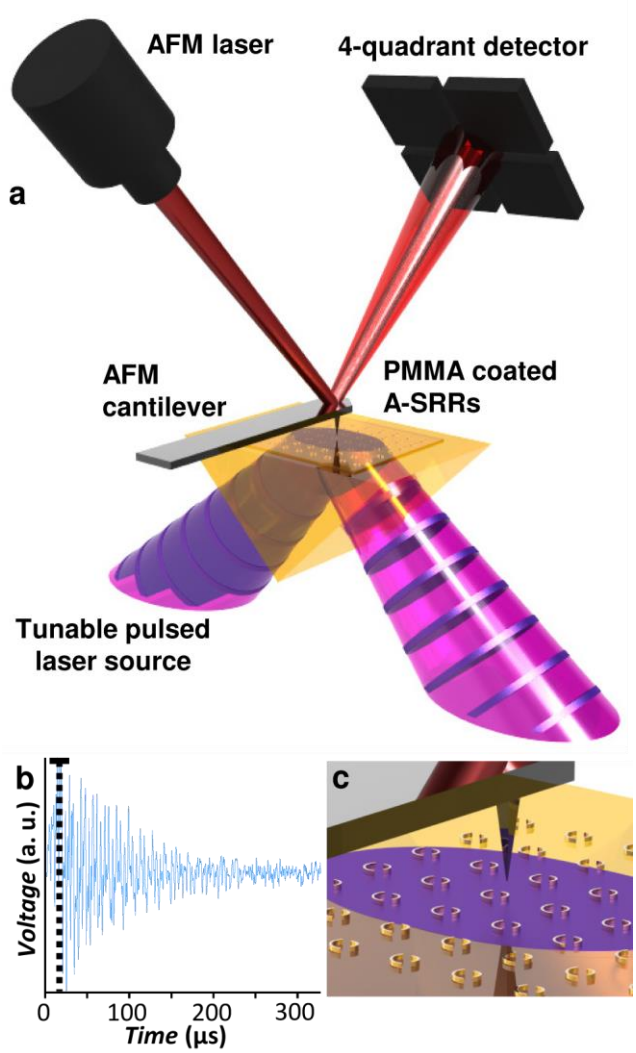

Figure 1. Schematic of the PTIR measurement. **a**, When IR laser pulses (purple) are absorbed by the sample (PMMA coating A-SRRs) it rapidly expands deflecting the AFM cantilever; the amplitude of the deflection, proportional to the absorbed energy, is measured by the AFM four-quadrant detector on a time scale much faster than the AFM feedback. The topography and the chemical (PTIR) signals are acquired by the 4-quadrant detector at different timescales preventing any possible crosstalk between the two channels. **b**, The PTIR signal is defined by the maximum of the peak to peak deflection during the cantilever ring down. **c**, The illuminated area beneath the AFM tip has a diameter of ≈ 30 μm. The tip is used to extract local IR spectrum. The total internal reflection geometry minimizes the light-tip direct interaction.

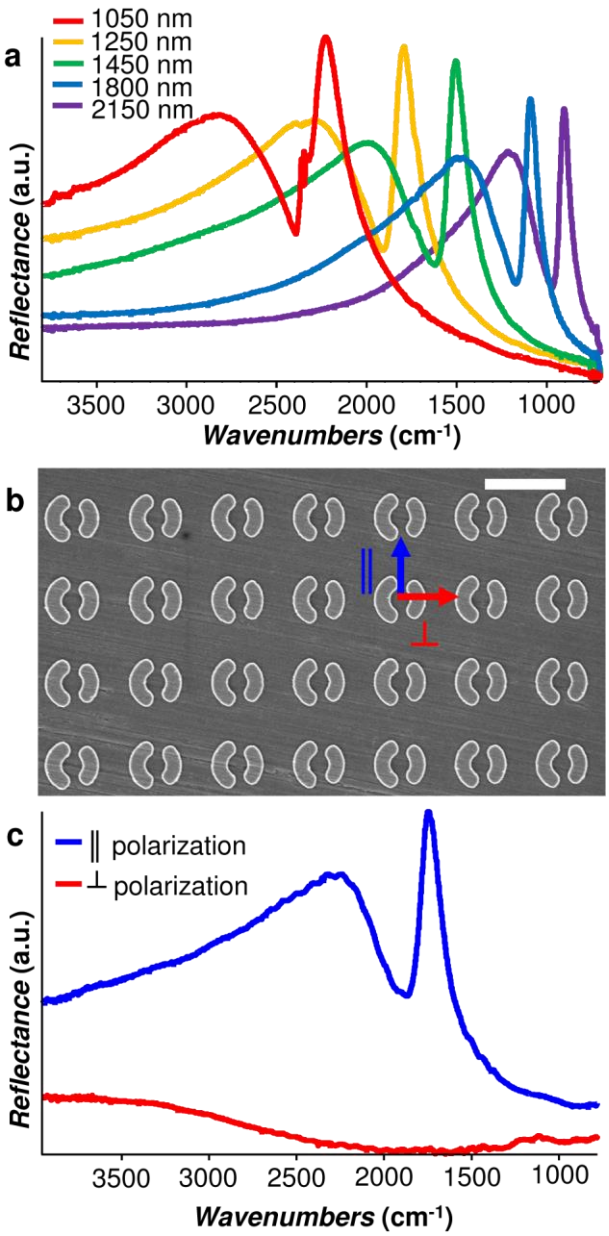

Figure 2. a, FTIR spectra of A-SRR arrays with different diameters showing that the A-SRRs' plasmonic resonances shift to longer wavelengths (smaller wavenumbers) as the diameter increases. **b**, Scanning Electron Microscopy (SEM) image for the ASRR-1300-d array (scale bar is 2 μm). The direction of the electric field for linear polarization in the FTIR spectra is indicated by a blue arrow in case of parallel polarization and by a red arrow in case of perpendicular

polarization. **c**, FTIR spectra for the ASRR-1300-d array recorded for parallel (blue) and perpendicular (red) linear polarization.

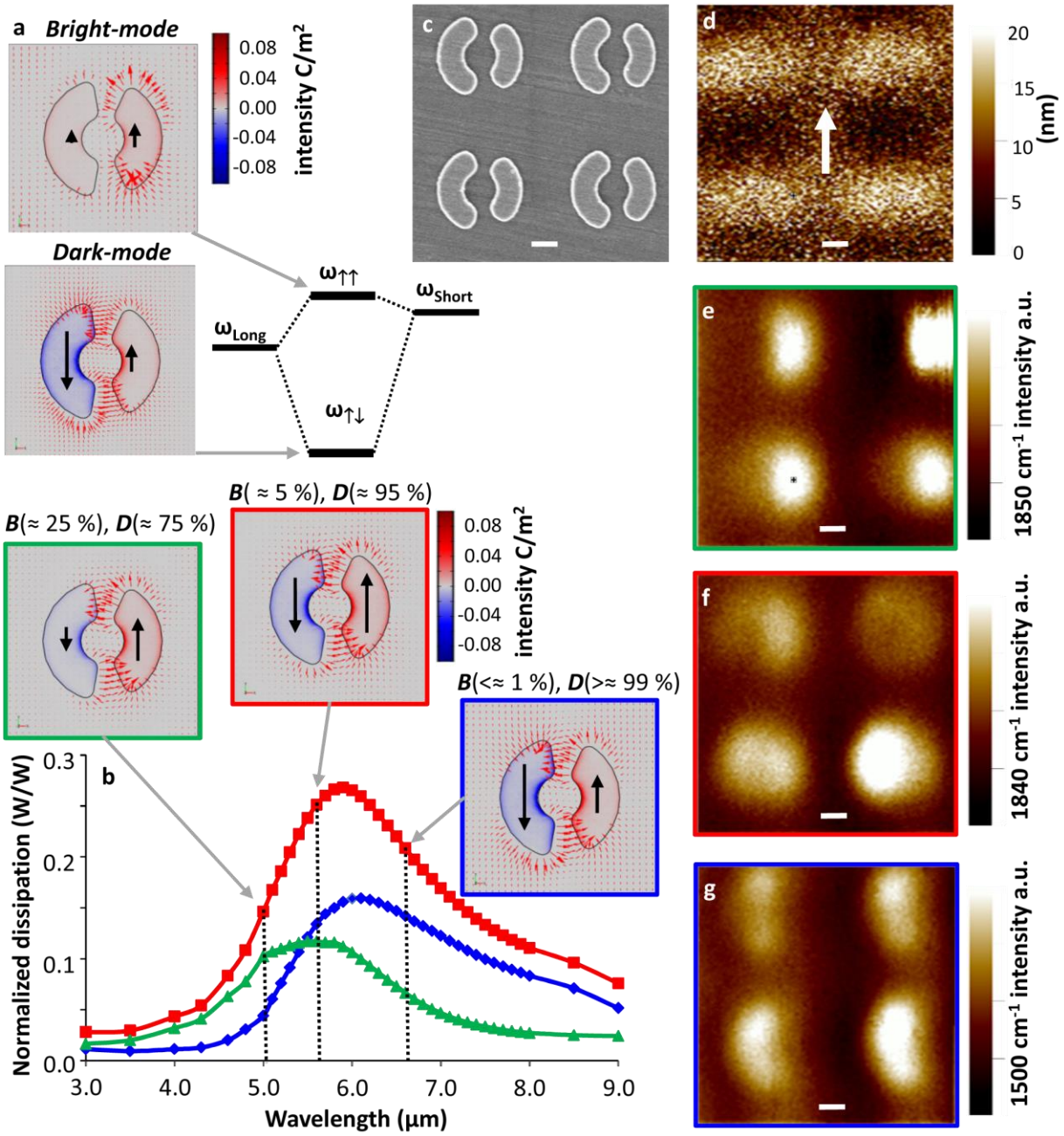

Figure 3. The ASRR-1300-d array, with a pitch of 1850 nm ± 35 nm, was coated with a 200 nm PMMA film. **a**, The fundamental resonances of the short and long arcs hybridize to form

symmetric (bright at 5.1 μm) and antisymetric (dark, at 6.0 μm) modes, as illustrated by the FEM results under top-down illumination. The red arrows denote electric field vectors; the color code is proportional to the (parallel) component of the electric polarization vector ($P_{\parallel}$), showing symmetric (antisymmetric) polarization corresponding to bright (dark) modes. The solid black arrows are proportional to the net parallel electric polarization (dipole moment) for each arc. **b**, FEM-calculated Ohmic dissipation in the short arc (green triangles), long arc (blue diamonds) and both arcs combined (red squares) normalized by the total optical power incident at 45° from the short arc side inside the ZeSe prism. The insets show the electric field and polarization. The net parallel polarization values for each arc (panel a) are used to define the basis vectors corresponding to the bright and dark modes. Net polarization values in panel b are then used to estimate the fractional excitation intensity attributable to the bright (*B*) and dark (*D*) modes. At longer wavelength (6.6 μm, blue inset) only the dark mode is excited ($D > 99$ %), in which a larger fraction of the optical power is dissipated by the longer arc. The crossover in the power dissipation between the two arcs is calculated at around 5.5 um (red inset). At shorter wavelengths (5.0 μm, green inset) a small admixture of the bright mode ($B \approx 25$ %) increases the power dissipated by the short arc and suppresses the power dissipated by the long arc. The calculation shows the very efficient excitation of the dark-mode under the conditions of PTIR experiment (> 25 % of incident power is absorbed by the gold resonators), attributed to a constructive combination of electric and magnetic dipolar coupling with the incident field. **c**, SEM image showing the size and spacing to scale with the AFM and PTIR images. Scale bar is 400 nm. **d**, AFM height image (the white arrow indicate the direction of the electric field polarization in the PTIR images), Scale bars are 400 nm. **e-g**, The PTIR images of the resonators excited at three different wavelengths confirm qualitatively the FEM predictions (b) showing the

crossover of the dissipated energy between the arcs. **e,** Excitation at 1850 cm^{-1} (5.41 μm) leads to the excitation of the dark-mode with an admixture of the bright-mode. Short arc excitation is enhanced and long arc excitation is suppressed by the mode interference. **f**, Excitation at 1840 cm^{-1} (5.43 μm) showing a smaller admixture of the bright-mode causing a similar contribution to the dissipation by the two arcs. **g**, Excitation at 1500 cm^{-1} (6.66 μm) showing that the dark-mode is excited almost exclusively. The excitation is mostly localized on the longer arc.

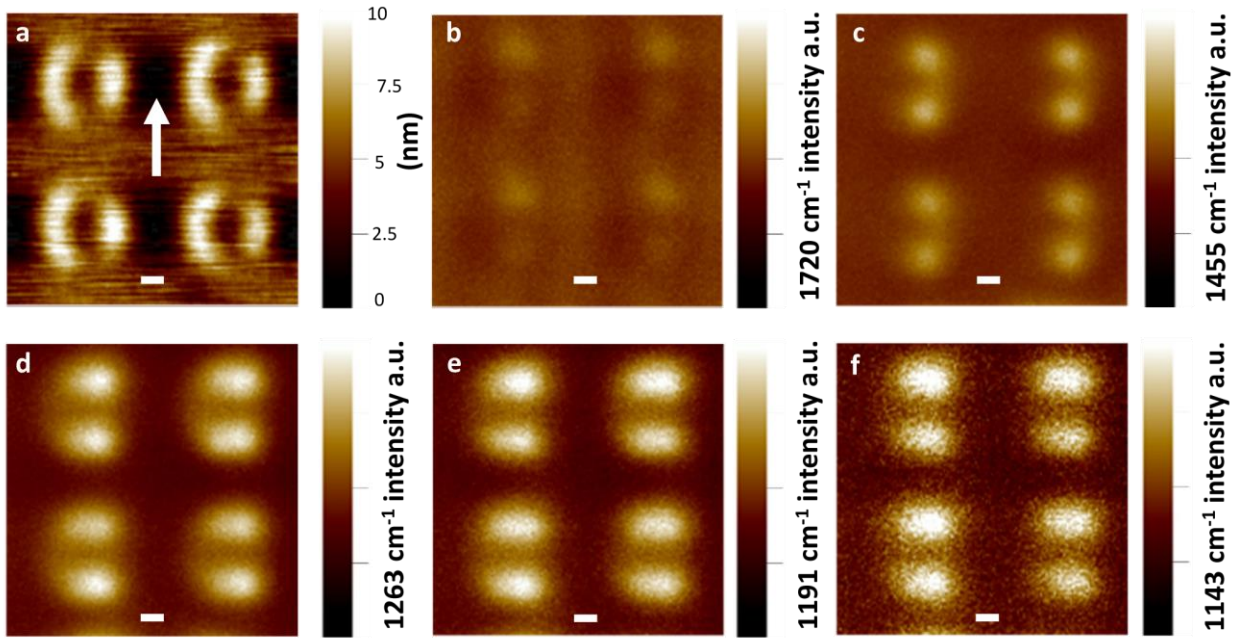

Figure. 4 a, AFM height image of ASRR-1700-d coated with a 200 nm PMMA film. (the white arrow indicate the direction of the electric field polarization in the PTIR experiments). The array pitch size is 2800 nm ± 35 nm. **b**, PTIR image of the PMMA carbonyl stretching mode at 1720 cm^{-1} (5.81 μm). **c**, PTIR image of PMMA CH_3 antisymmetric deformation mode at 1455 cm^{-1} (6.87 μm). **d**, PTIR image of PMMA C-O stretching vibrational mode at 1263 cm^{-1} (7.92 μm). **e**, PTIR image of the PMMA CH_3 wagging mode at 1191 cm^{-1} (8.40 μm). **f**, PTIR image of the PMMA CH_3 twisting mode at 1143 cm^{-1} (8.75 μm).[41] The PTIR signal is stronger when the

plasmon resonance overlaps with the PMMA absorptions. The PTIR images were obtained by illuminating the sample at 45° from the short arc side. The intensity scale of the PTIR images was normalized by the incident laser power; the scale bars are 500 nm.

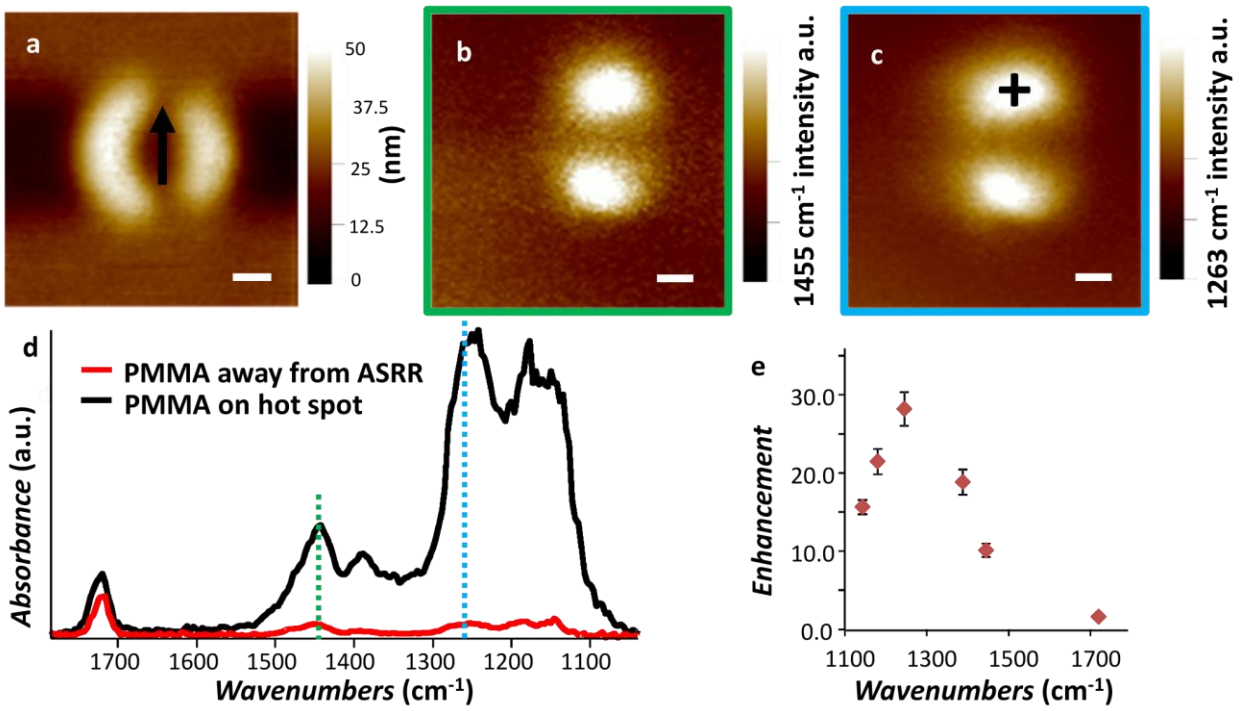

Figure 5. a, AFM height image ASRR-2000-10 coated with a 200 nm PMMA film (the black arrow indicate the direction of the electric field polarization). **b**, PTIR image of PMMA CH_3 antisymmetric deformation at 1455 cm^{-1} (6.87 µm). **c**, PTIR image of the PMMA C-O stretching vibration at 1263 cm^{-1} (7.92 µm).[41] **d**, PTIR spectra for PMMA recorded 300 µm away from the A-SRRs (red) and on the hot spot marked as "+" in figure 4c (black). The spectra are displayed in common scale. **e**, The SEIRA enhancement factor is defined as the ratio of the PMMA PTIR spectral intensity in the hot spot over the spectral intensity of PMMA recorded 300 µm away from the A-SRRs. SEIRA enhancement factors of 1.6, 10.1, 18.8, 28.2, 21.5 and 15.6 were calculated for PMMA peaks at 1720 cm^{-1}, 1445 cm^{-1}, 1263 cm^{-1}, 1190 cm^{-1} and 1143 cm^{-1},

respectively. The error bars represent a single standard deviation in the calculation of the PTIR enhancement factors from the PTIR spectral intensities. The PTIR images and spectra were obtained by illuminating the sample at 45° from the short arc side. The PTIR images are displayed with different intensity scale; the scale bars in the AFM and PTIR images are 500 nm.

Supporting Information. Additional A-SRRs FTIR spectra, nanofabrication scheme, SEM images, PTIR spectra and images as referenced in the main text. This material is available free of charge via the Internet at http://pubs.acs.org.

AUTHOR INFORMATION

Corresponding Author

*e-mail address: andrea.centrone@nist.gov

ACKNOWLEDGMENT

The authors acknowledge Rich Kasica of NIST for useful discussion on EBL and Dr. Doug Gotthard of Anasys Instruments for the help in setting up the polarization control module. A. C. acknowledges support from the National Institute of Standards and Technology American Recovery and Reinvestment Act Measurement Science and Engineering Fellowship Program, Award 70NANB10H026, through the University of Maryland. A. C. acknowledges support under the Cooperative Research Agreement between the University of Maryland and the National Institute of Standards and Technology Center for Nanoscale Science and Technology, Award 70NANB10H193, through the University of Maryland.

TOC FIGURE

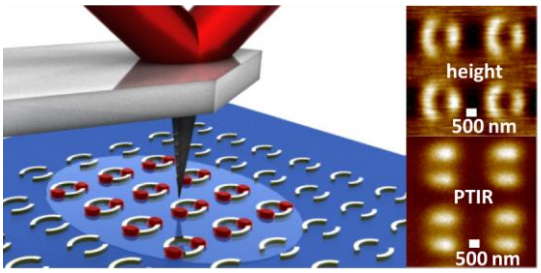

REFERENCES

1. Atwater, H. A.; Polman, A. *Nature Materials* **2010,** 9, (3), 205-213.
2. Stewart, M. E.; Anderton, C. R.; Thompson, L. B.; Maria, J.; Gray, S. K.; Rogers, J. A.; Nuzzo, R. G. *Chemical Reviews* **2008,** 108, (2), 494-521.
3. Anker, J. N.; Hall, W. P.; Lyandres, O.; Shah, N. C.; Zhao, J.; Van Duyne, R. P. *Nature Materials* **2008,** 7, (6), 442-453.
4. Lahiri, B.; Khokhar, A. Z.; De La Rue, R. M.; McMeekin, S. G.; Johnson, N. P. *Optics Express* **2009,** 17, (2), 1107-1115.
5. Hirsch, L. R.; Stafford, R. J.; Bankson, J. A.; Sershen, S. R.; Rivera, B.; Price, R. E.; Hazle, J. D.; Halas, N. J.; West, J. L. *Proceedings of the National Academy of Sciences of the United States of America* **2003,** 100, (23), 13549-13554.
6. Park, J. H.; von Maltzahn, G.; Ong, L. L.; Centrone, A.; Hatton, T. A.; Ruoslahti, E.; Bhatia, S. N.; Sailor, M. J. *Advanced Materials* **2010,** 22, (8), 880-885.
7. Kneipp, K.; Kneipp, H.; Itzkan, I.; Dasari, R. R.; Feld, M. S. *Chemical Reviews* **1999,** 99, (10), 2957-2975.
8. Doering, W. E.; Nie, S. M. *Journal Of Physical Chemistry B* **2002,** 106, (2), 311-317.
9. McFarland, A. D.; Young, M. A.; Dieringer, J. A.; Van Duyne, R. P. *Journal Of Physical Chemistry B* **2005,** 109, (22), 11279-11285.
10. von Maltzahn, G.; Centrone, A.; Park, J. H.; Ramanathan, R.; Sailor, M. J.; Hatton, T. A.; Bhatia, S. N. *Advanced Materials* **2009,** 21, (31), 3175-3180.
11. Le, F.; Brandl, D. W.; Urzhumov, Y. A.; Wang, H.; Kundu, J.; Halas, N. J.; Aizpurua, J.; Nordlander, P. *Acs Nano* **2008,** 2, (4), 707-718.
12. Adato, R.; Yanik, A. A.; Amsden, J. J.; Kaplan, D. L.; Omenetto, F. G.; Hong, M. K.; Erramilli, S.; Altug, H. *Proceedings of the National Academy of Sciences of the United States of America* **2009,** 106, (46), 19227-19232.
13. Wu, C. H.; Khanikaev, A. B.; Adato, R.; Arju, N.; Yanik, A. A.; Altug, H.; Shvets, G. *Nature Materials* **2012,** 11, (1), 69-75.
14. Pucci, A.; Neubrech, F.; Weber, D.; Hong, S.; Toury, T.; de la Chapelle, M. L. *Physica Status Solidi B-Basic Solid State Physics* **2010,** 247, (8), 2071-2074.
15. Chen, K.; Adato, R.; Altug, H. *Acs Nano* **2012,** 6, (9), 7998-8006.
16. Aouani, H.; Sipova, H.; Rahmani, M.; Navarro-Cia, M.; Hegnerova, K.; Homola, J.; Hong, M. H.; Maier, S. A. *Acs Nano* **2013,** 7, (1), 669-675.
17. Neubrech, F.; Pucci, A.; Cornelius, T. W.; Karim, S.; Garcia-Etxarri, A.; Aizpurua, J. *Physical Review Letters* **2008,** 101, (15), 157403.

18. Zentgraf, T.; Dorfmuller, J.; Rockstuhl, C.; Etrich, C.; Vogelgesang, R.; Kern, K.; Pertsch, T.; Lederer, F.; Giessen, H. *Optics Letters* **2008,** 33, (8), 848-850.
19. Bailo, E.; Deckert, V. *Chemical Society Reviews* **2008,** 37, (5), 921-930.
20. Yurtsever, A.; van der Veen, R. M.; Zewail, A. H. *Science* **2012,** 335, (6064), 59-64.
21. Alonso-Gonzalez, P.; Schnell, M.; Sarriugarte, P.; Sobhani, H.; Wu, C. H.; Arju, N.; Khanikaev, A.; Golmar, F.; Albella, P.; Arzubiaga, L.; Casanova, F.; Hueso, L. E.; Nordlander, P.; Shvets, G.; Hillenbrand, R. *Nano Letters* **2011,** 11, (9), 3922-3926.
22. Esteban, R.; Vogelgesang, R.; Dorfmuller, J.; Dmitriev, A.; Rockstuhl, C.; Etrich, C.; Kern, K. *Nano Letters* **2008,** 8, (10), 3155-3159.
23. Olmon, R. L.; Krenz, P. M.; Jones, A. C.; Boreman, G. D.; Raschke, M. B. *Optics Express* **2008,** 16, (25), 20295-20305.
24. Schnell, M.; Garcia-Etxarri, A.; Huber, A. J.; Crozier, K.; Aizpurua, J.; Hillenbrand, R. *Nature Photonics* **2009,** 3, (5), 287-291.
25. Hoffmann, J. M.; Hauer, B.; Taubner, T. *Applied Physics Letters* **2012,** 101, (19), 193105.
26. Cvitkovic, A.; Ocelic, N.; Hillenbrand, R. *Optics Express* **2007,** 15, (14), 8550-8565.
27. Dazzi, A.; Prazeres, R.; Glotin, E.; Ortega, J. M. *Optics Letters* **2005,** 30, (18), 2388-2390.
28. Marcott, C.; Lo, M.; Kjoller, K.; Prater, C.; Noda, I. *Applied Spectroscopy* **2011,** 65, (10), 1145-1150.
29. Dazzi, A.; Prazeres, R.; Glotin, F.; Ortega, J. M. *Ultramicroscopy* **2007,** 107, (12), 1194-1200.
30. Katzenmeyer, A. M.; Aksyuk, V.; Centrone, A. *Analytical Chemistry* **2013,** 85, (4), 1972-1979.
31. Lahiri, B.; Holland, G.; Centrone, A. *Small* **2013,** 9, (3), 439-445.
32. Dazzi, A.; Prazeres, R.; Glotin, F.; Ortega, J. M.; Al-Sawaftah, M.; de Frutos, M. *Ultramicroscopy* **2008,** 108, (7), 635-641.
33. Dazzi, A.; Glotin, F.; Carminati, R. *Journal of Applied Physics* **2010,** 107, (12), 124519
34. Debus, C.; Bolivar, P. H. *Applied Physics Letters* **2007,** 91, (18), 184102.
35. Fedotov, V. A.; Rose, M.; Prosvirnin, S. L.; Papasimakis, N.; Zheludev, N. I. *Physical Review Letters* **2007,** 99, (14), 147401.
36. Aydin, K.; Pryce, I. M.; Atwater, H. A. *Optics Express* **2010,** 18, (13), 13407-13417.
37. Lal, S.; Grady, N. K.; Kundu, J.; Levin, C. S.; Lassiter, J. B.; Halas, N. J. *Chemical Society Reviews* **2008,** 37, (5), 898-911.
38. Lahiri, B.; McMeekin, S. G.; De La Rue, R. M.; Johnson, N. P. *Applied Physics Letters* **2011,** 98, (15), 153116.
39. Graf, R. T.; Koenig, J. L.; Ishida, H. *Applied Spectroscopy* **1985,** 39, (3), 405-408.
40. Stanley, R. *Nature Photonics* **2012,** 6, (7), 409-411.
41. Lin-Vien, D.; Colthup, N. B.; Fately, W. G.; Grasselli, J. G., *handbook of infrared and raman characteristic frequencies of organic molecules*. Academic Press: Boston, 1991.

Supporting information

Nanoscale Imaging of Plasmonic Hot Spots and Dark Modes with the Photothermal Induced Resonance Technique

Basudev Lahiri[1, 2], Glen Holland[1], Vladimir Aksyuk[1] and Andrea Centrone [1, 2]*

[1]NIST, Center for Nanoscale Science and Technology, Gaithersburg, 100 Bureau Drive, MD 20899 (USA)
[2]University of Maryland, Institute for Research in Electronics and Applied Physics (IREAP), College Park, MD 20742 (USA)
*Corresponding Author e-mail: Andrea.Centrone@nist.gov

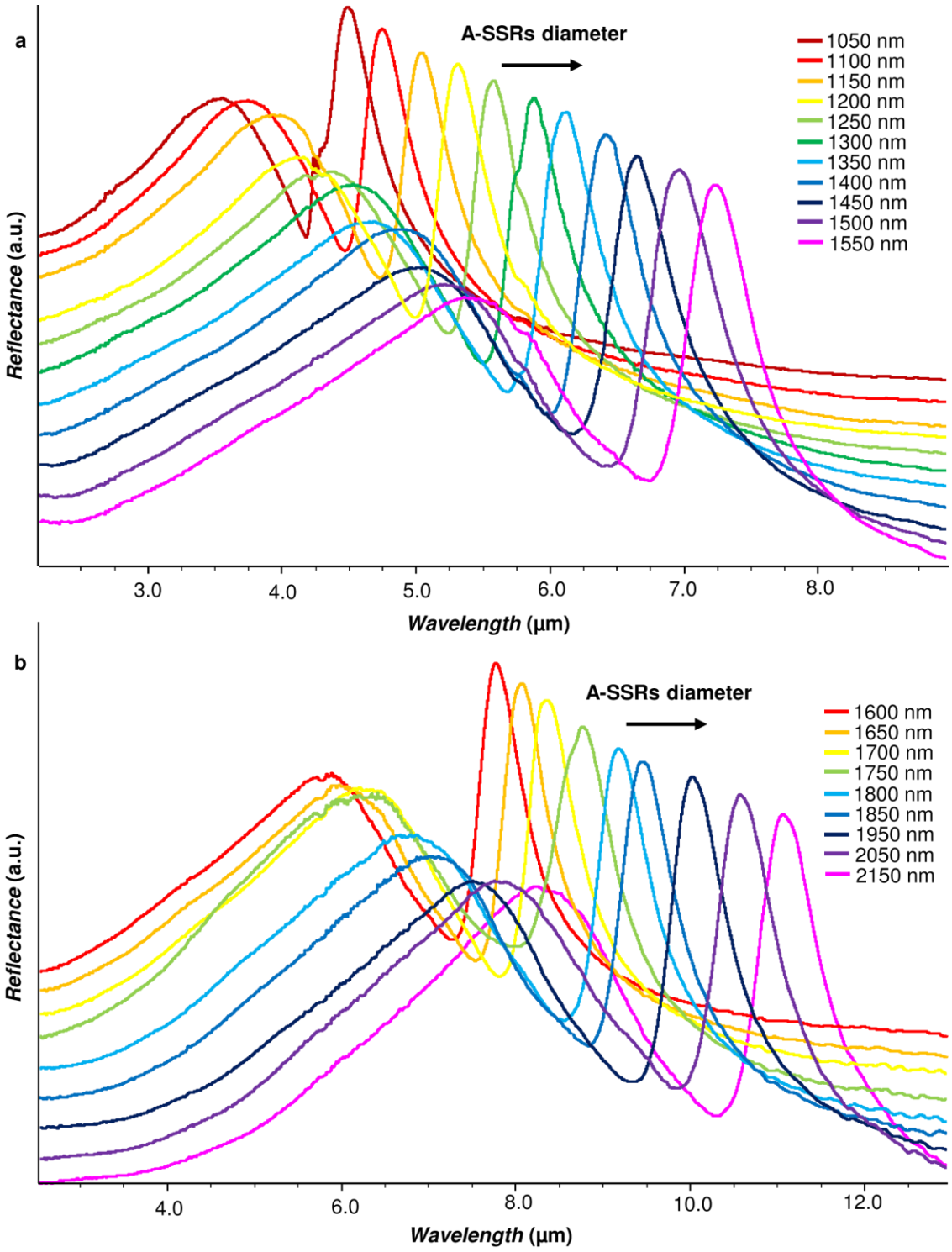

Figure S1. FTIR spectra of A-SRRs arrays as a function of the resonators external diameter. The spectra were recorded with parallel polarization and are displayed with an offset for clarity.

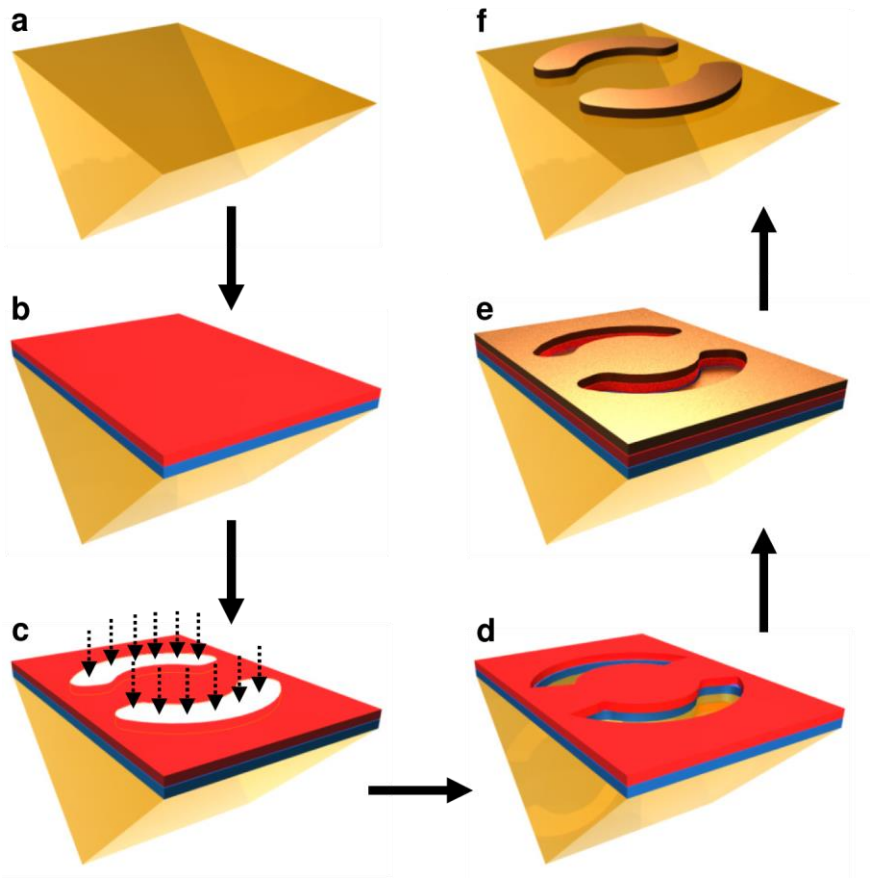

Figure S2. Nanofabrication scheme: a) A ZnSe right angle prism is used as a substrate for the A-SRRs fabrication, b) a PMMA bilayer (250 nm and 350 nm) was spun on the ZnSe prism, c) the A-SRRs arrays are written with electron beam lithography, d) the pattern is developed with MIBK and IPA e) electron beam deposition is used to deposit a 5 nm chromium adhesion layer and a 150 nm gold layer, f) The A-SRRs arrays are obtained after lift of in hot acetone.

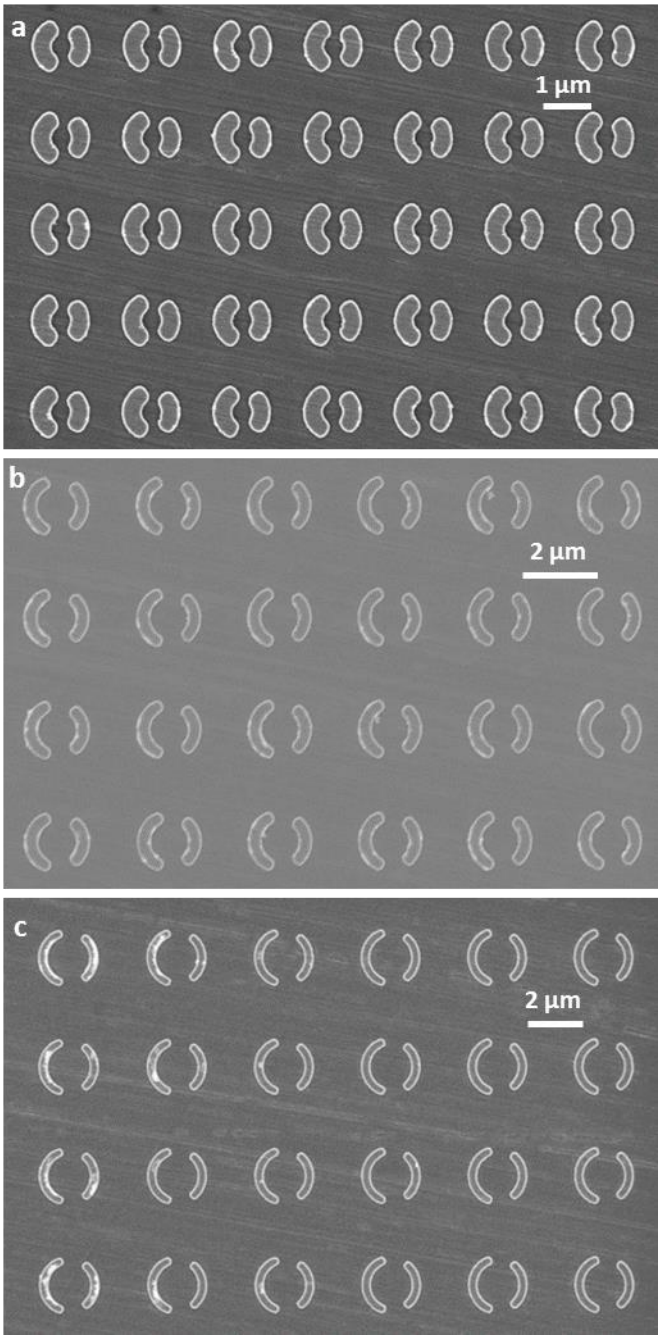

Figure S3. SEM images for A-SRRs arrays with pitch twice the resonators diameter: a) ASRR-1200-d, b) ASRR-1700-d, c) ASRR-2150-d. Scale bars are indicated in each image.

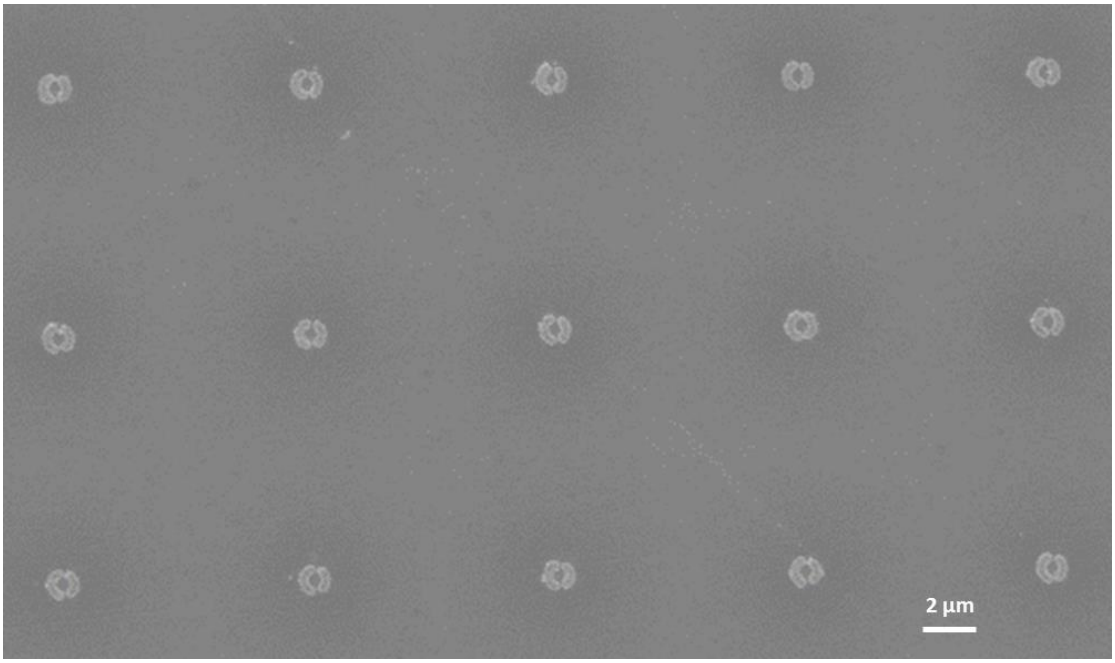

Figure S4. SEM images for ASRR-1250-10 array with 10 µm pitch.

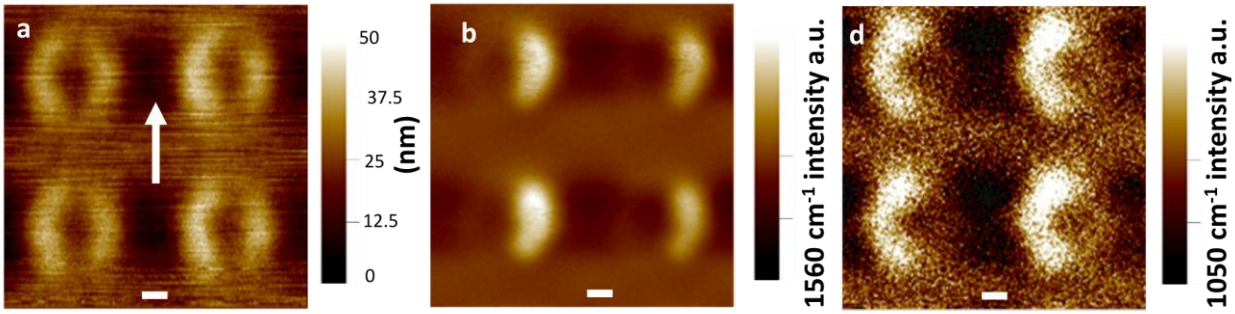

Figure S5. PTIR images (parallel polarization) of the plasmonic modes for A-SRR-1700-d coated with 200 nm of PMMA. **a**, AFM height image (the white arrow indicate the direction of the electric field polarization in the PTIR experiments), **b**, Excitation at 1560 cm^{-1} (6.41 µm) showing that the mode is mostly localized on the shorter arc (the shorter arc excitation is enhanced and the longer arc excitation is suppressed by the bright and dark mode interference). **c**, Excitation at 1050 cm^{-1} (9.52 µm) showing that the mode is mostly localized on the longer arc. The images scale bars are 500 nm.

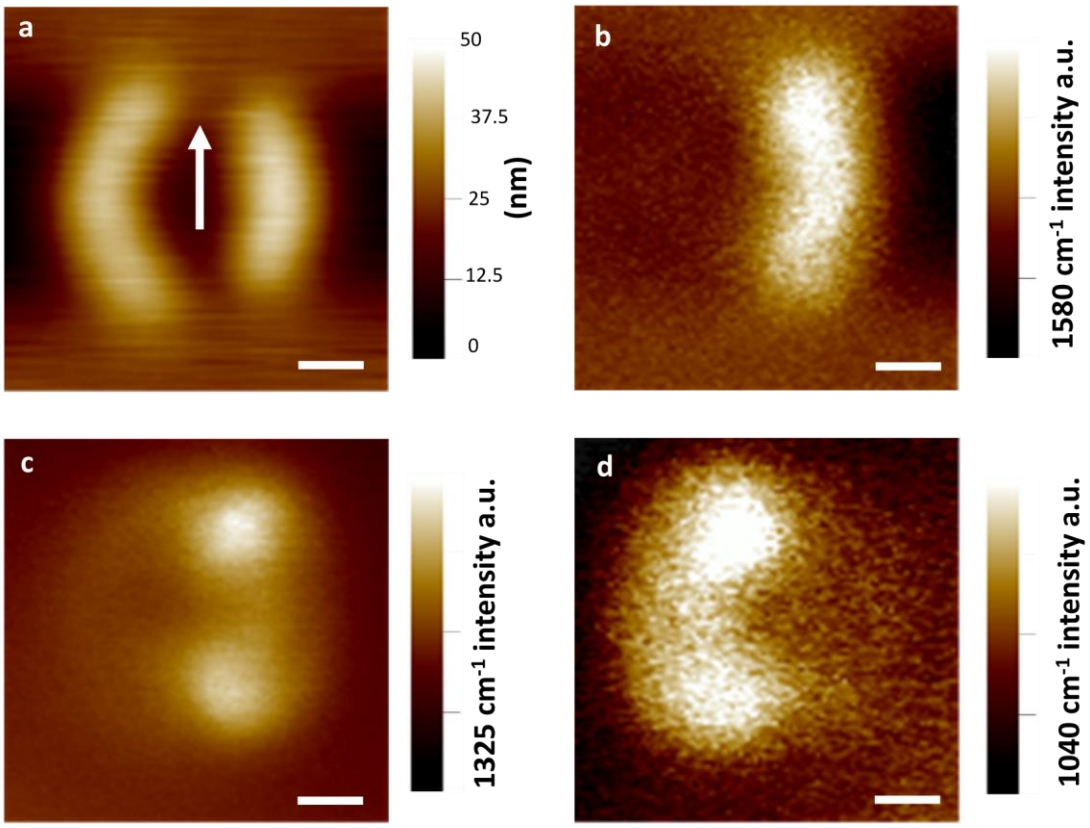

Figure S6. PTIR images (parallel polarization) of the plasmonic modes for A-SRR-1650-d coated with 200 nm of PMMA. **a**, AFM height image (the white arrow indicate the direction of the electric field polarization in the PTIR experiments), **b**, Excitation at 1580 cm^{-1} (6.33 µm) showing that the mode is mostly localized on the shorter arc (the shorter arc excitation is enhanced and the longer arc excitation is suppressed by the bright and dark mode interference). **c**, Excitation at 1235 cm^{-1} (8.10 µm) showing that when the light is absorbed both by PMMA and by the plasmonic modes the PTIR image is dominated by PMMA absorption due to the large absorption enhancement in the near field hotspots. The faint halo surrounding the hot spots is due the plasmonic modes close to the crossover wavelength for the energy dissipated in the 2 arcs. **c**, Excitation at 1040 cm^{-1} (9.61 µm) showing that the mode is mostly localized on the longer arc. The images scale bars are 500 nm.

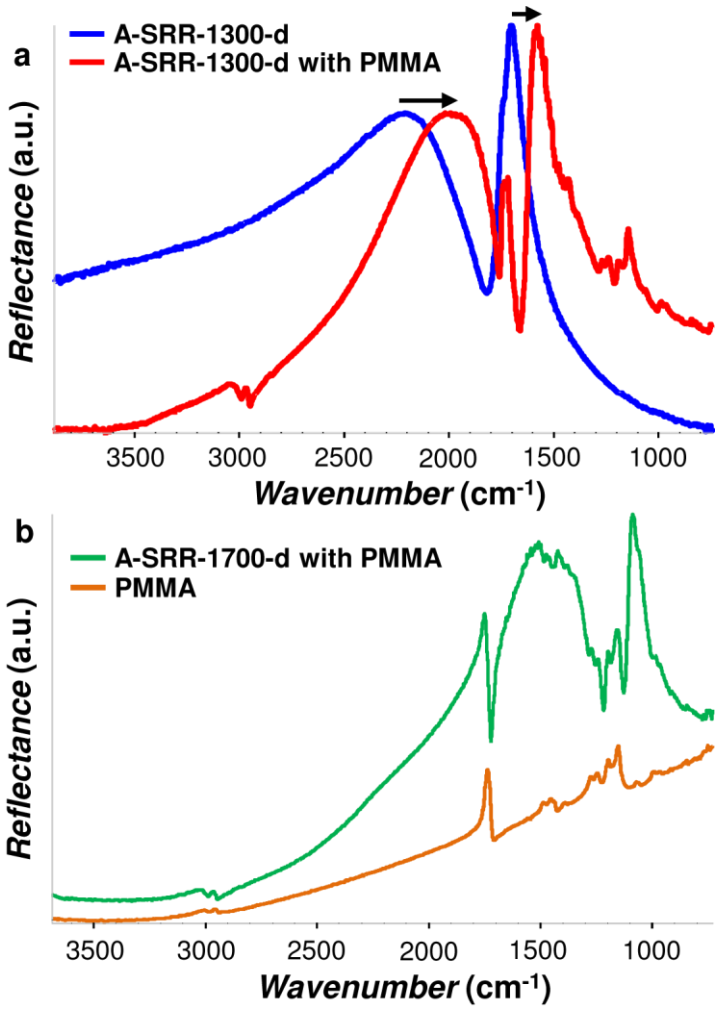

Figure S7. SEIRA FTIR spectra. a. ASRR-1300-d FTIR spectra the bare array (blue) and for the array coated by a 200 nm PMMA layer (red); the PMMA refractive index causes a shift of the resonators plasmonic peaks (black arrows). **b**, PMMA (orange) and PMMA coated ASRR-1700-d (green) FTIR spectra; the plasmon resonances enhance the absorption, shift and distort the PMMA vibrational peaks in the reflection spectrum (SEIRA effect). All spectra were recorded for parallel polarization.

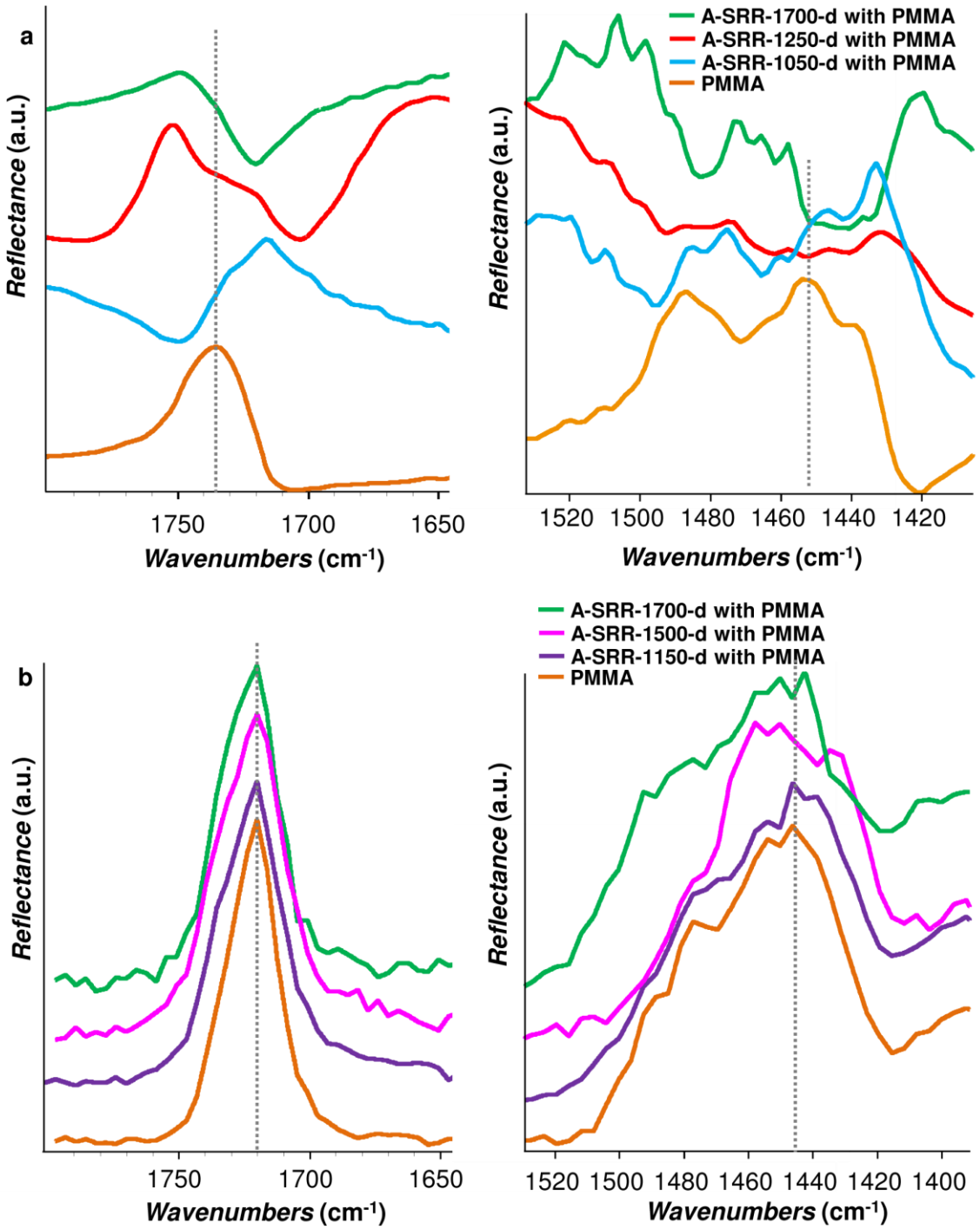

Figure S8. Surface enhanced FTIR and PTIR spectra comparison for A-SRRs array coated with 200 nm PMMA. a. Zoomed in FTIR spectra for PMMA (orange), ASRR-1050-d (light blue), ASRR-1250-d (red) and ASRR-1700-d (green) showing the spectral distortion typical of Fano interference. b. Zoomed in PTIR spectra for PMMA (orange), ASRR-1150-d (light purple), ASRR-1500-d (pink) and ASRR-1700-d (black) showing that PTIR absorption spectra are in first approximation not distorted by Fano interference. Spectra are displayed with an offset for clarity.

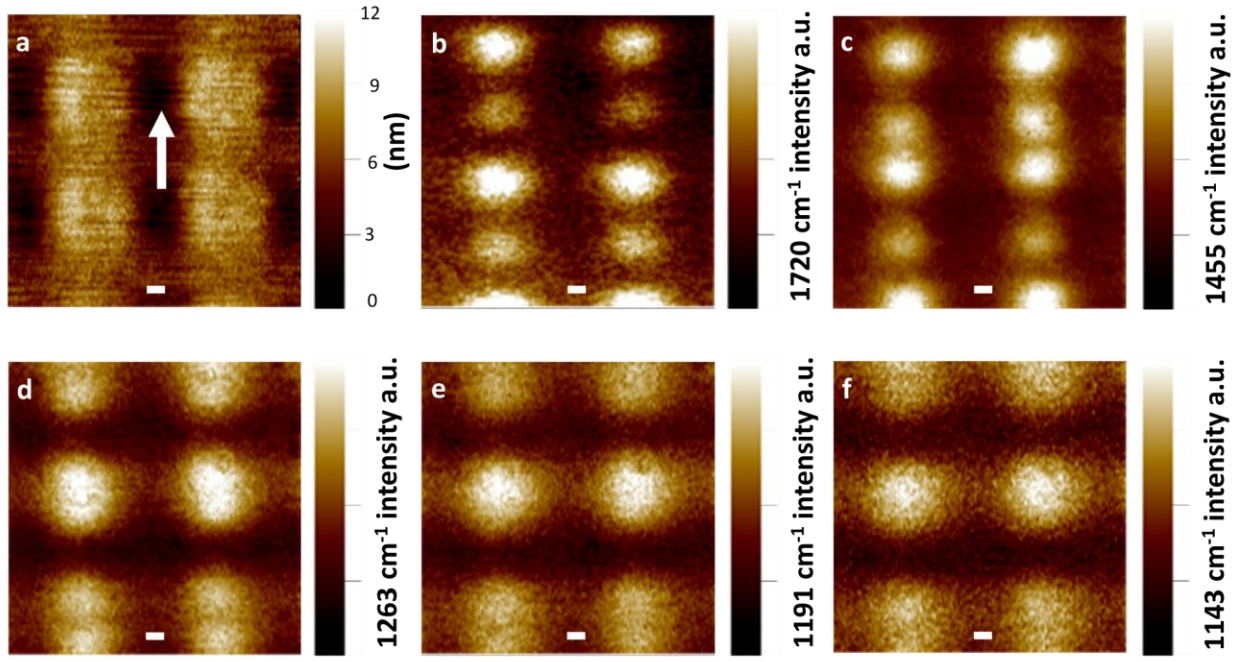

Figure S9. **PTIR images (parallel polarization) of SEIRA hot-spots for A-SRR-1150-d coated with 200 nm of PMMA. a**, AFM height image (the white arrow indicate the direction of the electric field polarization in the PTIR experiments) The array pitch size is 2050 nm ± 35 nm. **b**, PTIR image of the PMMA carbonyl stretching vibration at 1720 cm^{-1} (5.81 µm). **c**, PTIR image of PMMA CH_3 antisymmetric deformation at 1455 cm^{-1} (6.87 µm). **d**, PTIR image of PMMA C-O stretching at 1263 cm^{-1} (7.92 µm). **e**, PTIR image of the PMMA CH_3 wagging vibration at 1191 cm^{-1} (8.40 µm). **f**, PTIR image of the PMMA CH_3 twisting vibration at 1143 cm^{-1} (8.75 µm).[41] The PTIR images and spectra were obtained by illuminating the sample at 45° from the short arc side. The PTIR images are displayed with different intensity scale. The images scale bars are 250 nm.

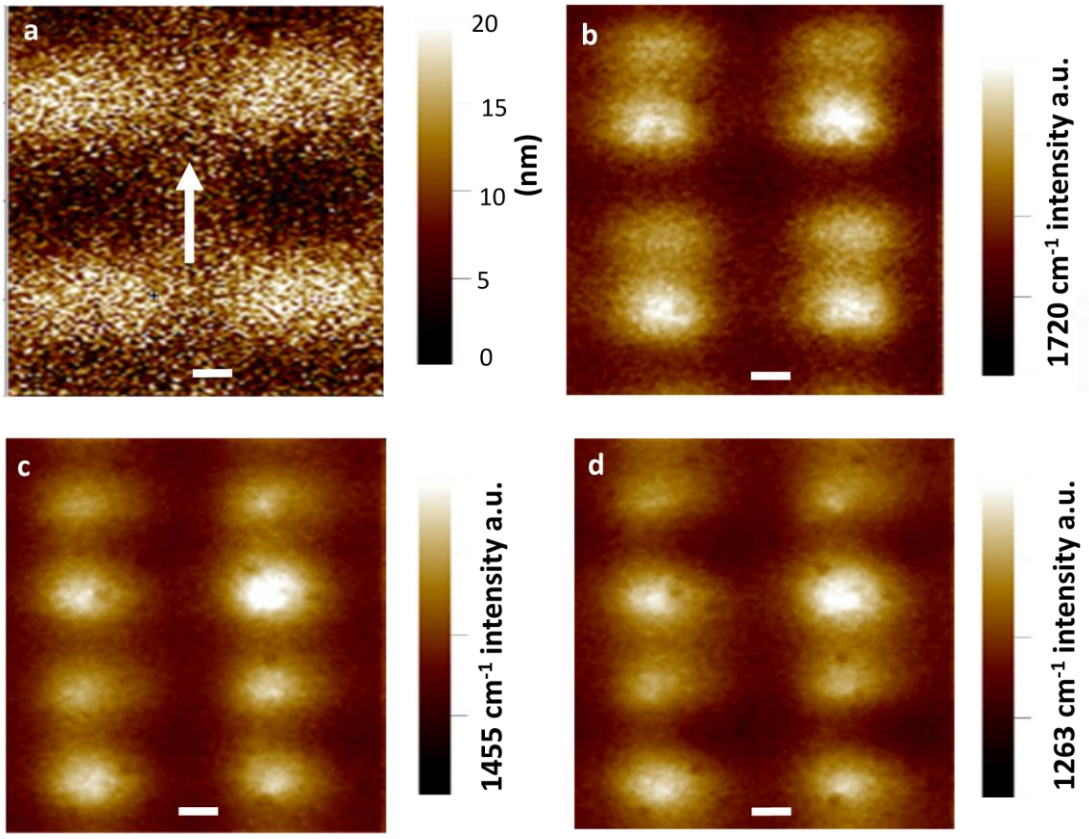

Figure S10. PTIR images (parallel polarization) of SEIRA hot-spots for A-SRR-1300-d coated with 200 nm of PMMA. a, AFM height image (the white arrow indicate the direction of the electric field polarization in the PTIR experiments). **b**, PTIR image of the PMMA carbonyl stretching vibration at 1720 cm^{-1} (5.81 µm). **c**, PTIR image of PMMA CH_3 antisymmetric deformation at 1455 cm^{-1} (6.87 µm). **d**, PTIR image of PMMA C-O stretching at 1263 cm^{-1} (7.92 µm). The PTIR images and spectra were obtained by illuminating the sample at 45° from the short arc side. The PTIR images are displayed with different intensity scale. The images scale bars are 400 nm.

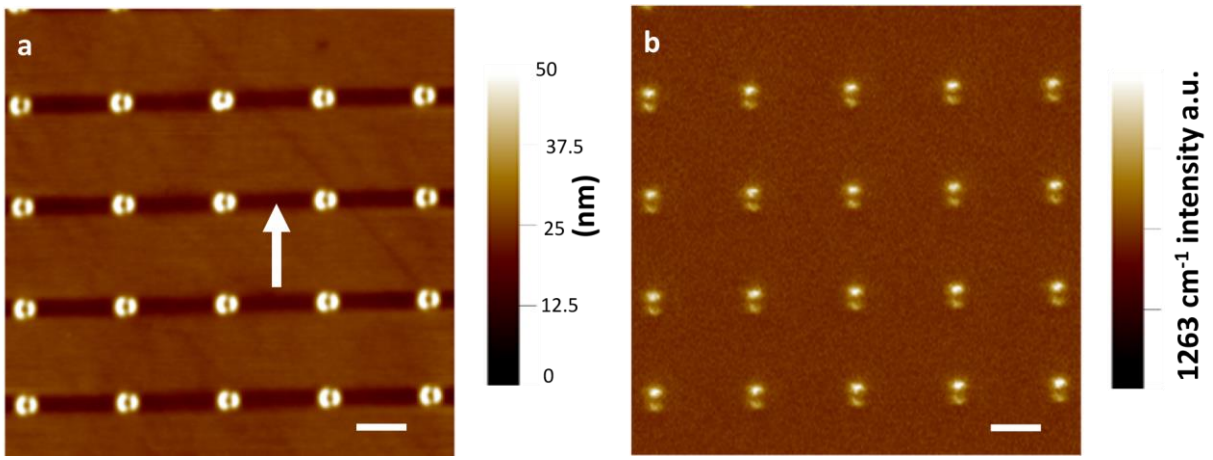

Figure S11. Large area (45 µm x 45 µm) PTIR image (parallel polarization) of SEIRA hot-spots for ASRR-2000-10 coated with a 200 nm PMMA film. **a**, AFM height image (the white arrow indicate the direction of the electric field polarization). **b**, PTIR image of the PMMA C-O stretching vibration at 1263 cm^{-1} (7.92 µm). The PTIR images and spectra were obtained by illuminating the sample at 45° from the short arc side. The scale bars are 5000 nm and the pixel size is 100 nm by 100 nm.

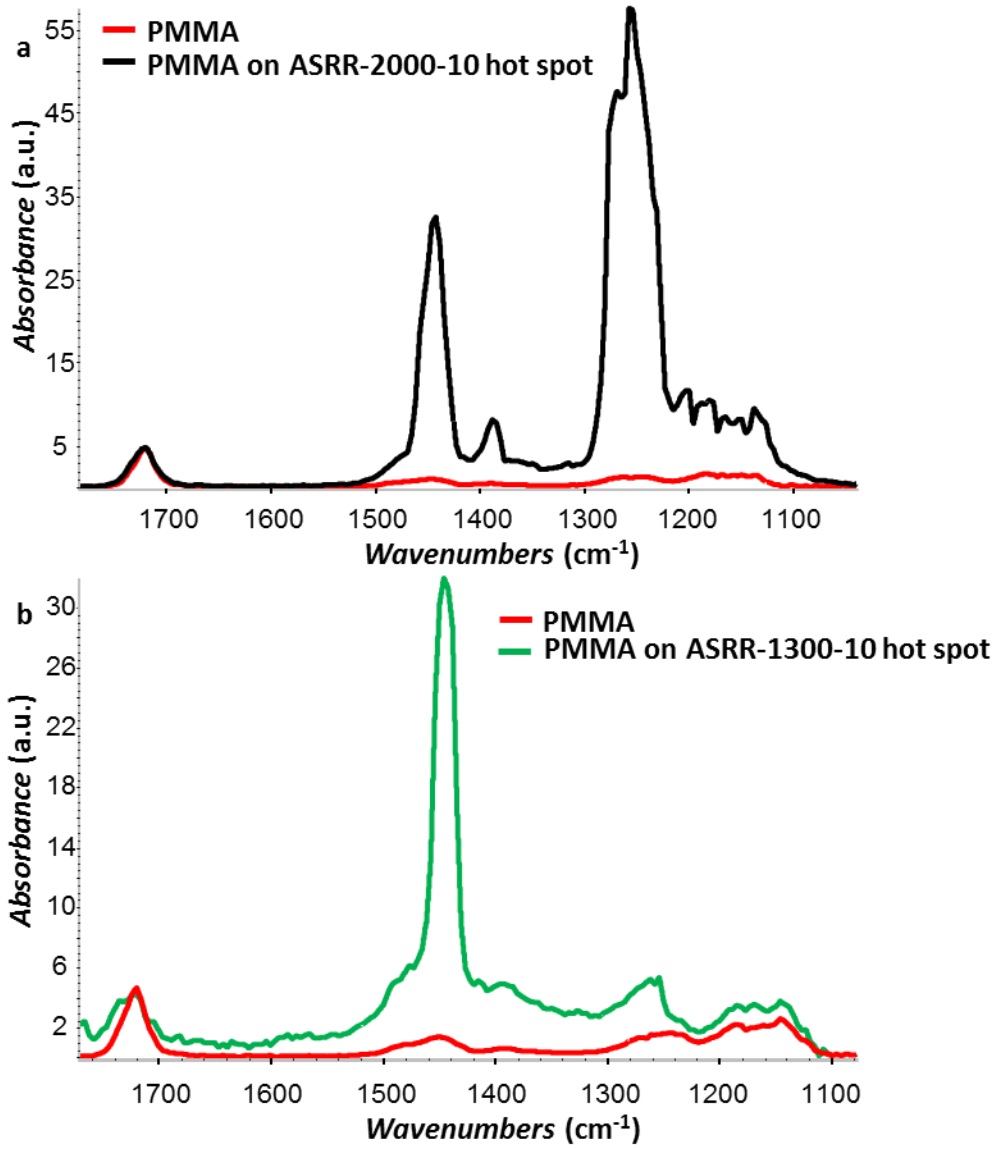

Figure S12. PTIR spectra (parallel polarization) of bare PMMA and SEIRA hot-spots obtained with laser power up to 1 µJ per pulse. a, SEIRA enhancement up to 55 was recorded for A-SRR-2000-10. **b**, SEIRA enhancement up to 24 was recorded for A-SRR-1300-d**.** The spectra in each panel are displayed on a common scale.

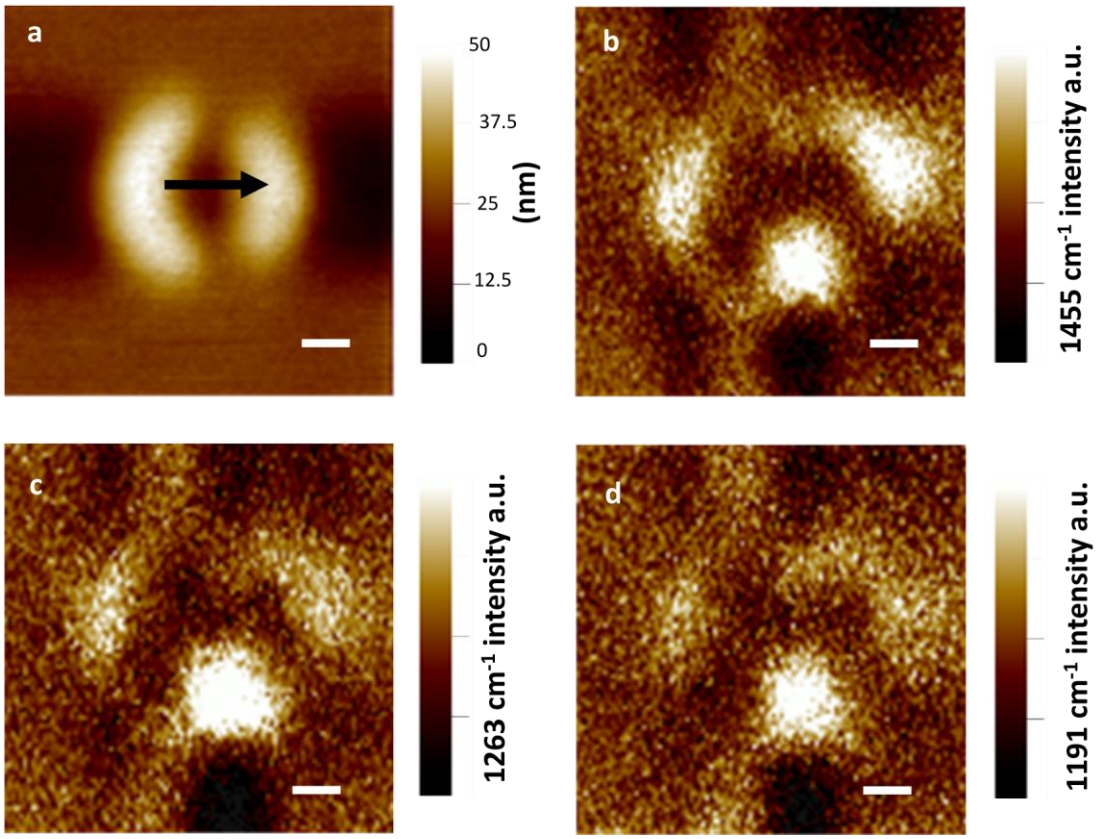

Figure S13. SE-PTIR images (perpendicular polarization) of hot-spots for A-SRR-2000-10 coated with 200 nm of PMMA. **a**, AFM height image (the black arrow indicate the direction of the electric field polarization). **b**, PTIR image of PMMA CH_3 antisymmetric deformation at 1455 cm^{-1} (6.87 µm). **c**, PTIR image of PMMA C-O stretching vibration 1263 cm^{-1} (7.92 µm). **d**, PTIR image of the PMMA CH_3 wagging vibration at 1191 cm^{-1} (8.40 µm). The PTIR images and spectra were obtained by illuminating the sample at 45° from the hot spot side. Scale bars are 500 nm.

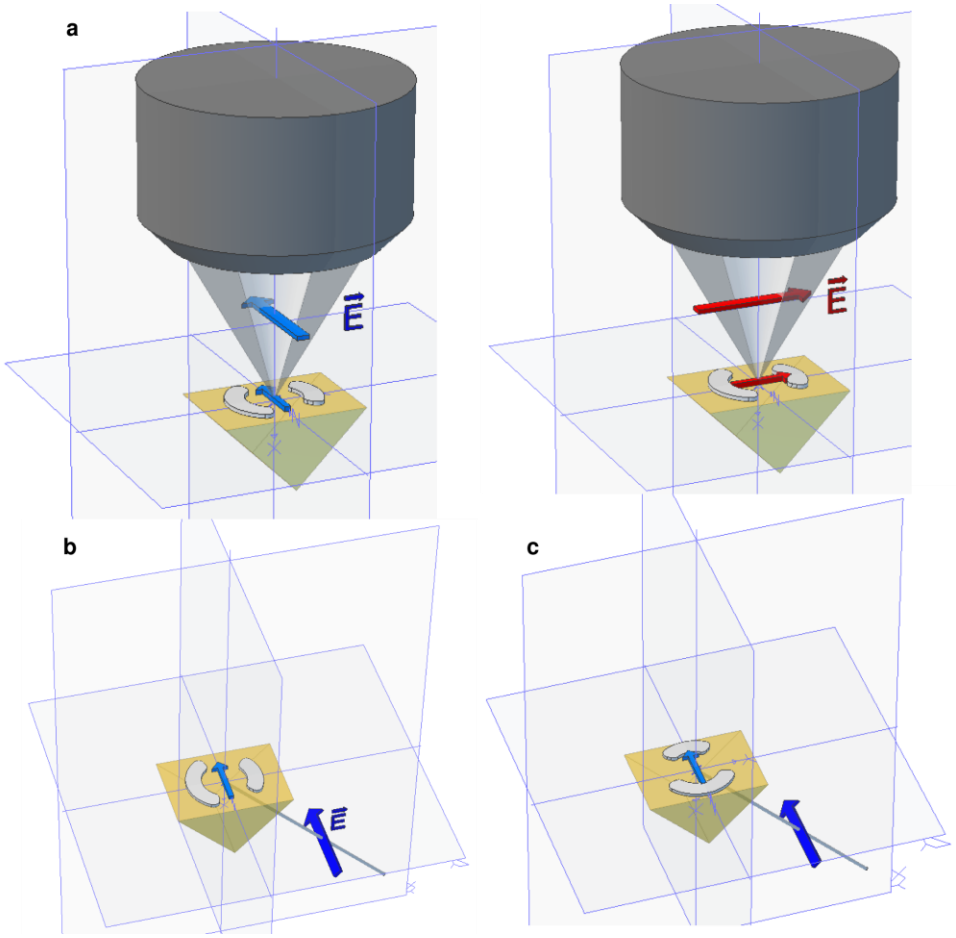

Figure S14. Sketches of the linearly polarized FTIR and PTIR experiments. a, FTIR experiments were obtained at normal incidence by focusing the light by means of a microscope reverse Cassegrain objective (36x) which illuminate and collects light with incidence angles between 15° to 30° with respect to the sample surface normal (the light between normal incidence and 15° is blocked by the objective). The polarization at the sample was selected by using a wire grid polarizer (not shown) to be either parallel (blue) or perpendicular (red). **b**, PTIR experiments were obtained at 45° incidence illuminating the sample from the short arc side. The polarization at the sample was controlled by using a wire grid polarizer and a polarization control module consisting of 3 mirrors (not shown). The blue arrow depicts the electric field vector with parallel polarization mentioned in the text. **c**, The perpendicular polarization experiments mentioned in the text were obtained on A-SRRs structures fabricated rotated by 90° instead of rotating the light polarization by 90°.